Quantitative Comparison of Modular Linear Permanent Magnet Vernier Machines with and without Partitioned Primary[*]

Yunpeng Xu, Jinghua Ji[*], Zhijian Ling, Chen Wang and Wenxiang Zhao

(School of Electrical and Information Engineering, Jiangsu University, Zhenjiang 212013, China)

Abstract: A comparison of two modular linear permanent-magnet vernier (LPMV) machines is presented. A modular LPMV machine with a partitioned primary, which can significantly improve the modulation effect, is proposed. Benefitting from the partition design, the space conflict between the permanent magnet (PM) and the armature magnetic field is relieved. First, the topologies of modular LPMV machines with and without a partitioned primary are presented. Then, the effect of the partitioned primary on the modular LPMV machine is analyzed using flux modulation theory. Moreover, analytical expressions for the trapezoidal permeance are derived. In addition, the harmonic components, back electromotive forces, and thrust forces of the machines with and without the partitioned primary are comparatively analyzed. The results reveal that the thrust force density of the LPMV machine with a partitioned primary is increased by 32.3%. Finally, experiments are performed on a prototype machine for validation.

Keywords: Linear permanent magnet machine, partitioned primary, flux modulation theory, modular structure

Nomenclature

P_{PM}	Number of PM arrays
P_s	Number of effective modulating teeth
P_w	Number of pole pairs of the armature windings
L_m	Distance between adjacent primary modules (mm)
k	A positive integer
τ_s	Secondary pole pitch of the two machines (mm)
F	Magnetomotive force
F_0	DC component of the magnetomotive force
F_i	i^{th} harmonic component of the magnetomotive force
i, j	$0, 1, 2, \cdots, \infty$
N_s	Number of elementary units
L	Effective length of the secondary (mm)
F_{PM}	Amplitude of the magnetomotive force waveform
x	Airgap position (mm)
θ	Magnetization angle of the obliquely magnetized PMs
a	Width of the obliquely magnetized PMs (mm)
b	Width of the radially magnetized PMs (mm)
v	Speed of the primary (m/s)
t	Time (ms)
Λ	Permeance coefficient
Λ_0	DC component of the permeance
Λ_j	Harmonic component of the permeance
x_0	Initial airgap position (mm)
c_1, c_2	Widths of the teeth and slots in the secondary of the LPMV machine without the partitioned primary
d_1	Width of the gap between the upper ends of the secondary of the LPMV machine with the partitioned primary
d_2	Width of the lower ends of the secondary of the LPMV machine with the partitioned primary
Λ_e, Λ_h	Length between the maximum and minimum permeance
Λ_f, Λ_l	Minimum permeance
B	Airgap flux density
m	$1, 3, 5, \cdots, \infty$
N_m	Harmonic component of the winding function
L_{stk}	Axial lamination length of the two machines
N_p	Numbers of armature winding turns
k_w	Winding factor

Yunpeng Xu et al.: Quantitative Comparison of Modular Linear Permanent Magnet Vernier Machines
with and without Partitioned Primary

73

1　Introduction

Owing to their advantages with regard to cost and manufacturing, linear induction machines have been successfully used in long-stroke applications, such as light rails and maglev trains [1-4]. However, the electrical and mechanical energy conversion rates are relatively low. With the development of permanent magnet (PM) materials, linear PM machines can address this problem [5-8]. However, conventional linear PM machines are expensive because their armature windings or PMs are mounted on long secondaries.

Linear primary PM machines have been proposed [9-12]. Both the PMs and armature windings of the linear primary PM machine are mounted on the short primary, whereas the long secondary is composed of only the iron core. Compared with conventional linear PM machine, this structure can significantly reduce the number of PMs and coils; thus, the cost is significantly reduced in long-stroke applications. Linear primary PM machines can be divided into linear flux PM machines [13-14], linear flux-switching PM machines [15-16], and linear PM vernier (LPMV) machines [17-18]. Owing to their advantages, such as a relatively simple topology and small thrust force ripple, LPMV machines have attracted increasing attention. However, conventional LPMV machines suffer from a significant leakage flux of the PMs, resulting in a relatively low thrust force density. To address this issue, a PM array was proposed [19] that combined the advantages of Halbach and consequent-pole PM arrays [20-21]. This not only reduces the number of PMs but also increases the thrust force.

In recent years, it has been verified that a modular design can improve the fault-tolerant capability [22-23], where the mutual inductance between phases is optimized by adjusting the distance between unit modules. However, the influence of the modular design on the modulation effect cannot be ignored. The modular design has undesirable effects. For example, each module generates a new detent force, resulting in a large thrust-force ripple. This reduces the back electromotive force (back EMF). Therefore, it is necessary to propose a modular structure that does not degrade the machine performance.

Moreover, regarding the topology of the existing modular LPMV machine, the armature windings and PMs are located in the same primary [24-25]. This structure leads to accelerated crowding of the PM and armature magnetic fields. Therefore, it is difficult to increase the thrust force density. A partitioned primary can solve this problem [26-28]. It splits the primary into two parts, allowing the armature windings and PMs to be located in different parts. The thrust force and reliability of the machine can be improved by combining a partitioned primary design with a modular design. However, whether this conforms to the modulation mechanism requires further study. A comparison of the flux-modulation effects between modular LPMV machines with and without a partitioned primary is insufficient. Using flux modulation theory, the influence of the partitioned primary on LPMV machines can be effectively analyzed.

In this study, modular LPMV machines with and without a partitioned primary were compared. The internal mechanism of the improved modulation effect was analyzed from the perspective of harmonics. The remainder of this paper is organized as follows. Section 2 introduces the topologies of the two LPMV machines. In Section 3, the magnetomotive force (MMF)-permeance models of the two LPMV machines are derived. The analytical results for the airgap flux density are then compared with the results of the finite-element method (FEM). In Section 4, the harmonic amplitudes, back EMFs, and thrust forces of the two machines are compared and analyzed. A prototype machine was built and tested to verify the accuracy of the theoretical analyses, as described in Section 5. Finally, conclusions are drawn in Section 6.

2　Topology explanation

The topologies of the modular LPMV machines with and without a partitioned primary are shown in Fig. 1. In contrast to the machine without a partition, a machine with a partition splits the primary into two separate parts, where the PMs and armature windings are spatially isolated. Therefore, a machine with a partition can solve the problem of insufficient thrust force density without a partition. The armature windings and PMs were located in the primaries of the two machines. These topologies are suitable for long-term stroke applications because of their low costs. The magnetization directions of the PM

arrays are shown in Fig. 1. The use of the PM array not only reduces flux leakage but also assists the middle PMs in generating the main flux, thereby increasing the PM utilization rate. The amount of PMs in the two machines was kept the same to ensure that their magnetic loads were identical.
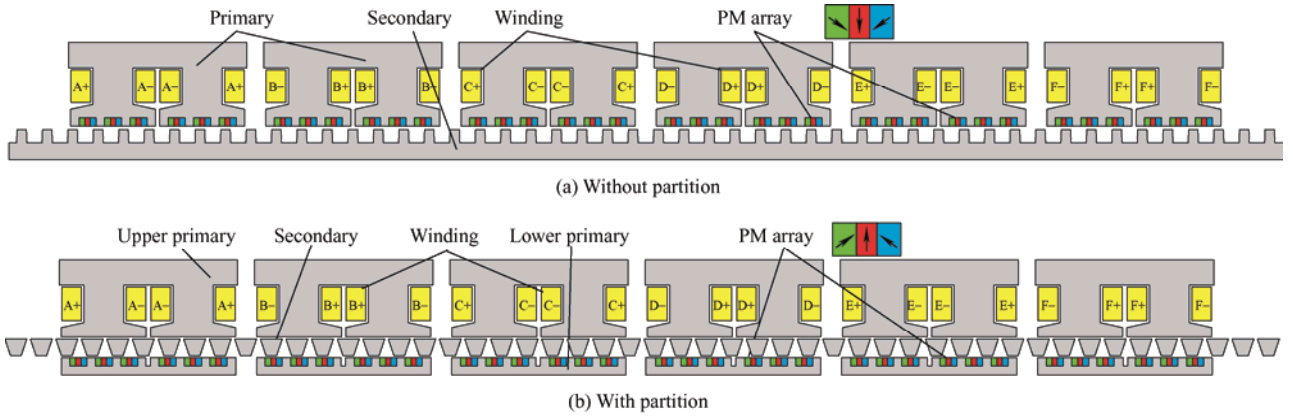

(a) Without partition

(b) With partition

Fig. 1   Configurations of the LPMV machines

A secondary machine with a partitioned primary has an inverted trapezoidal structure, as shown in Fig. 1b, where the upper end of the trapezoidal structure is longer than the lower end. Compared with traditional structures, the inverted trapezoidal structure has the advantage of less flux leakage in the lower airgap, which improves the electromagnetic performance.

To satisfy the modulation relationship, the two machines adopt a modular primary design. The requirements for the modular primary design are shown in Fig. 2. Because of the offset between the modules, the electrical angle between phases changes. Therefore, a symmetric six-phase back EMF can be obtained using a modular primary design. To satisfy the operating mechanism, the distance between adjacent primary modules L_m can be expressed as follows

$$L_m = \left(\frac{k}{2} \pm \frac{1}{6} \right) \tau_s \tag{1}$$

where k represents a positive integer, and τ_s represents the secondary pole pitch.

(a) Primary

(b) Secondary of the machine without a partition
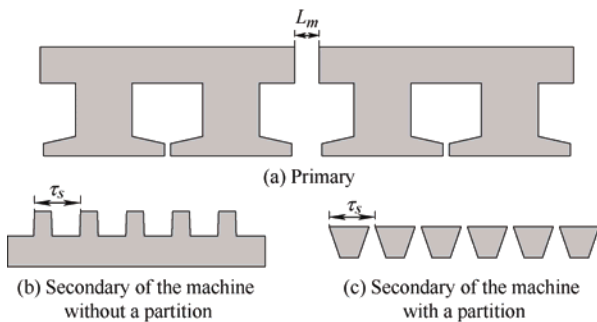
(c) Secondary of the machine with a partition

Fig. 2   Modular design parameters of the two machines

The two linear machines adopt the same winding connections, as shown in Fig. 3. To obtain symmetric six-phase no-load back EMFs, the two coils in each phase should be connected in opposite directions. The phase-angle difference between phase windings is 60°, whereas the difference between adjacent modules is 120°. In addition, the numbers of winding turns and load currents are the same for the two machines. Therefore, the electrical loads are identical.
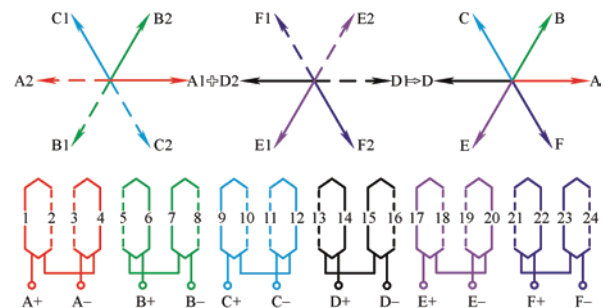

Fig. 3   Winding structures of two machines

The design parameters of the two machines are presented in Tab. 1. A machine with a partition has two layers of airgaps. To ensure that the airgap reluctances of the two machines are the same, the overall airgap lengths of the two machines are the same. In addition, for a fair comparison, the same materials and electromagnetic loads are used for the two machines.

The two machines conform to flux modulation theory. The relationship among the number of PM arrays P_{PM}, the number of effective modulating teeth P_s, and the number of pole pairs of the armature windings P_w is given as follows

Yunpeng Xu et al.: Quantitative Comparison of Modular Linear Permanent Magnet Vernier Machines
with and without Partitioned Primary

75

$$P_w = |P_s - P_{PM}| \qquad (2)$$

To achieve a stable and continuous thrust force, the speed of the primary magnetic field should be equal to that of the armature magnetic field. In addition, the PM pole pair should be consistent with that of the modulated armature magnetic field. Therefore, the speed of the working flux can be expressed as follows

$$v_{PM} = \frac{P_s}{P_w} v \qquad (3)$$

$$G = \frac{P_s}{P_w} \qquad (4)$$

where G, v, and v_{PM} represent the modulation ratio, mechanical speed, and airgap magnetic field speed, respectively.

Tab. 1　Design specifications of the two machines

Parameter	Without partition	With partition
Primary pole pitch/mm	52.5	
Primary length/mm	680	
Primary slot opening/mm	2	
Secondary pole pitch/mm	15	
Width of the secondary spilt teeth/mm	5	
Thickness of PMs/mm	5	
Width of obliquely magnetized PMs/mm	3.5	
Angle of obliquely magnetized PMs/(°)	35	
Width of horizontally magnetized PMs/mm	3	
Overall airgap length/mm	2	
Width of upper end of secondary teeth/mm	5	13
Width of lower end of secondary teeth/mm	6	
Lamination material	DW315_50	
PM material	NdFe35	
Rated current/A	5	
Rated speed/(m/s)	1.5	
Number of PM arrays	36	
Number of secondary teeth	42	
Number of turns per coil	100	

3　Effect of partitioned primary

3.1　PM MMF

The open-circuit airgap flux density of LPMV machines with and without a partitioned primary can be calculated using the MMF and permeance models. Before establishing the MMF model, the following assumptions should be made: ① the magnetic permeability of the iron core is infinite, ② the airgap magnetic field only varies in the x-axis direction, ③

the PM MMF is a square wave, and ④ there is no PM MMF in the horizontal direction. The salient teeth and the PMs of the primary teeth were considered in the MMF model, and the salient teeth of the secondary were considered in the permeance model. Therefore, the analytical model can fully capture the effect of the partitioned primary on flux modulation.

Fig. 4 shows the PM MMF waveform in one module of the two machines. The PM MMF contains 12 elementary units, each of which can be regarded as one period. Because consequent-pole PM arrays are used, the salient teeth at both ends can be considered to have opposite polarities. For the airgap flux density, the MMF models are the same because the two machines have the same PM distribution. According to Fig. 4, the Fourier expression of the PM MMF for the two LPMV machines can be expressed as follows

$$F(x) = F_0 + \sum_{i=1}^{\infty} F_i \cos\left(2\pi i \frac{N_s}{L} x\right) \qquad (5)$$

$$\begin{cases} F_0 = N_s F_{PM} \dfrac{b}{L} + 2N_s F_{PM} \sin\theta \dfrac{2a}{L} \\ F_i = \dfrac{2F_{PM} + 2\sin\theta F_{PM}}{\pi i} \sin\left(\pi i N_s \dfrac{b + 2a\sin\theta}{L}\right) \cdot \\ \quad \sum_{k=1}^{12} (-1)^{k+1} \cos\left[\pi i N_s (2k-1)\dfrac{a+b}{L}\right] \end{cases} \qquad (6)$$

where a and b represent the widths of the obliquely and radially magnetized PMs, respectively, and θ represents the magnetization angle of obliquely magnetized PMs in the horizontal direction.

As shown in Fig. 4, four consecutive salient teeth and three sets of PM arrays form an elementary unit. Each elementary unit can be regarded as a period. Therefore, the two machines have N_s periods. The spatial harmonics of the PM MMF are shown in Fig. 5. As shown, the PM MMF of the two machines is mainly composed of iN_sth-order harmonics, where i represents positive integers.

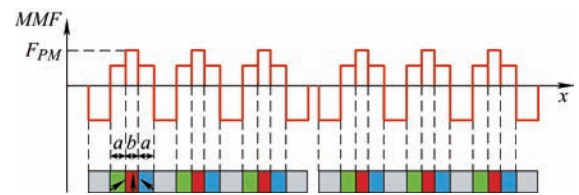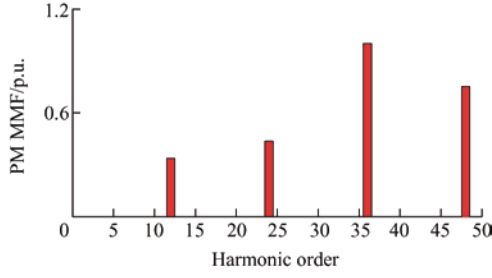

Fig. 4　PM MMF model of the two machines

Fig. 5   Spatial harmonics of the PM MMF

3.2   Permeance

Fig. 6 shows the permeance waveforms of the two LPMV machines. Because of the effect of the partitioned primary, the secondary shapes of the two machines differ. Therefore, the permeance models of the two machines differ significantly. In addition, the machine with a partitioned primary has two layers of airgaps; the paths of the flux lines from the armature winding side and the PM side are different. Therefore, the permeance models of the upper and lower airgaps differ. The primary part of the machine moves at speed v in the positive direction of the x-axis. The corresponding permeance model can be expressed as

$$\Lambda(x,t) = \Lambda_0 + \sum_{j=1}^{\infty} \Lambda_j \cos\left[jP_s \frac{2\pi}{L}(x - x_0 - vt) \right] \quad (7)$$

(a) Without partition
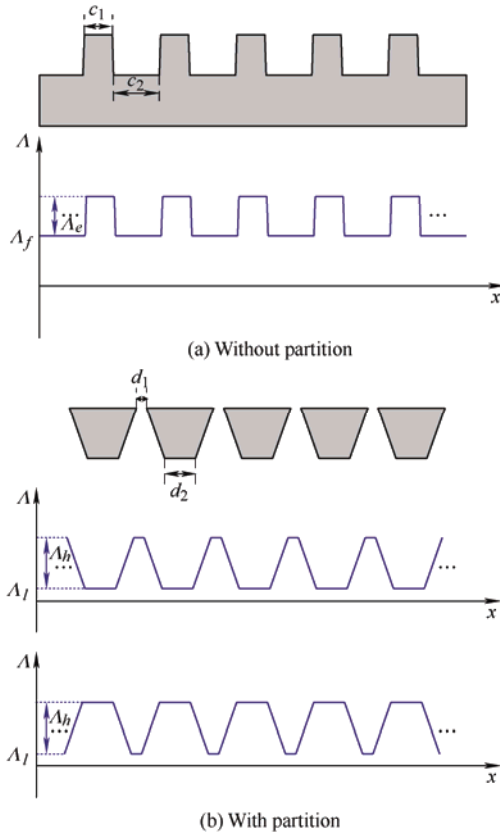

(b) With partition

Fig. 6   Permeance models of the two machines

where L represents the effective length of the secondary teeth, P_s represents the number of effective modulating teeth, and x_0 represents the initial airgap position.

(1) Permeance of the machine without a partitioned primary. According to Fig. 6a, the permeance model of the machine can be expressed as

$$\begin{cases} \Lambda_0 = \dfrac{P_s}{L_0}\left(c_1 \Lambda_e + c_2 \Lambda_f\right) \\ \Lambda_j = \dfrac{2}{j\pi}\left(\Lambda_e - \Lambda_f\right)\sin\left(jc_1 P_s \dfrac{\pi}{L}\right) \end{cases} \quad (8)$$

(2) Permeance of the machine with a partitioned primary. According to Fig. 6b, the permeance model of the upper airgap can be expressed as

$$\begin{cases} \Lambda_0 = \dfrac{P_s}{L}\left(d_1 \Lambda_h + d_2 \Lambda_l\right) \\ \Lambda_j = \dfrac{2}{j\pi}\left(\Lambda_h - \Lambda_l\right)\sin\left(jd_1 P_s \dfrac{\pi}{L}\right) \end{cases} \quad (9)$$

The permeance model of the lower airgap can be expressed as

$$\begin{cases} \Lambda_0 = \dfrac{P_s}{L}\left(d_2 \Lambda_h + d_1 \Lambda_l\right) \\ \Lambda_j = \dfrac{2}{j\pi}\left(\Lambda_h - \Lambda_l\right)\sin\left(jd_2 P_s \dfrac{\pi}{L}\right) \end{cases} \quad (10)$$

3.3   Airgap flux density

The effect of the partitioned primary on the LPMV machine was analyzed using flux modulation theory. The airgap flux density was calculated by multiplying the PM MMF by the effective airgap magnetic permeance. Therefore, the no-load airgap flux densities of the two LPMV machines can be expressed as follows

$$B(x,t) = F(x)\Lambda(x,t) =$$
$$F_0 \Lambda_0 + \Lambda_0 \sum_{i=1}^{\infty} F_i \cos\left(iN_s \frac{2\pi}{L}x\right) +$$
$$\sum_{i=1}^{\infty}\sum_{j=1}^{\infty} F_i \Lambda_j \frac{\cos\alpha + \cos\beta}{2} +$$
$$F_0 \sum_{j=1}^{\infty} \Lambda_j \cos\left[jP_s \frac{2\pi}{L}(x - x_0 - vt) \right] \quad (11)$$

$$\begin{cases} \alpha = (iN_s + jP_s)\dfrac{2\pi}{L}x - jP_s \dfrac{2\pi}{L}(x_0 + xt) \\ \beta = (iN_s - jP_s)\dfrac{2\pi}{L}x + jP_s \dfrac{2\pi}{L}(x_0 + vt) \end{cases} \quad (12)$$

For calculating the flux densities of the different airgaps, Λ_0 and Λ_j were calculated using Eqs. (8)-(10). From Eq. (10), it can be predicted that there exist

Yunpeng Xu et al.: Quantitative Comparison of Modular Linear Permanent Magnet Vernier Machines
with and without Partitioned Primary

77

harmonics of order iN_s, jP_s, and $|iN_s \pm jP_s|$ ($i, j = 1, 2, 3, \cdots$) for both airgap flux densities.

According to the above analysis, the harmonic orders of the airgap flux densities of the two machines were identical. Owing to the effect of the partitioned primary, the amplitudes of these harmonics were completely different. The airgap flux density and its harmonic spectrum for the two machines were predicted and verified via theoretical analysis and the FEM, as shown in Figs. 7-9.
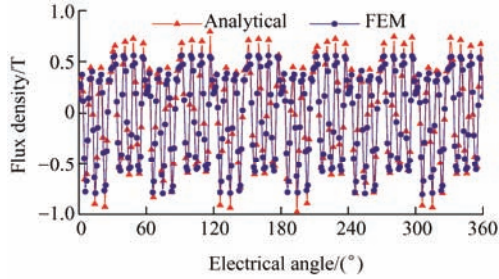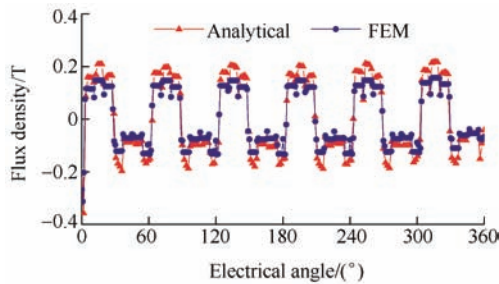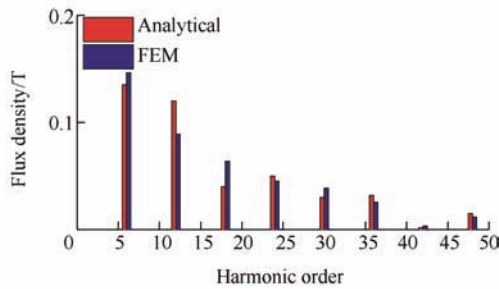

(a) Waveform
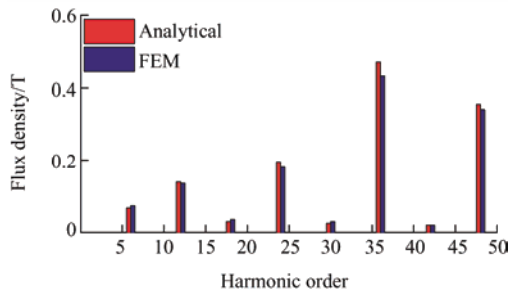
(b) Harmonic spectra

Fig. 7 Comparison of the airgap flux densities of the machine without a partitioned primary obtained via two methods
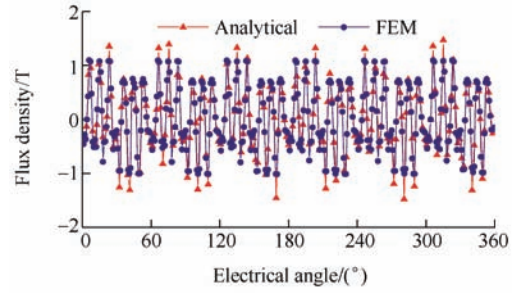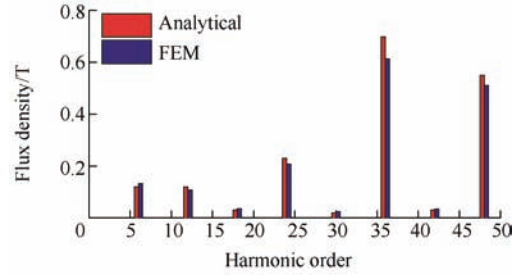

(a) Waveform

(b) Harmonic spectra

Fig. 8 Comparison of the upper airgap flux densities of the machine with a partitioned primary obtained via two methods

(a) Waveform

(b) Harmonic spectra

Fig. 9 Comparison of the lower airgap flux densities of the machine with a partitioned primary obtained via two methods

4 Performance analysis

In this section, modular LPMV machines with and without a partitioned primary are quantitatively analyzed and compared using the FEM. The key dimensions and specifications are presented in Tab. 1.

4.1 Modulation effect

Fig. 10 presents the open-circuit airgap flux densities of the two machines. As shown, the harmonic orders of the two machines were identical. Owing to the improved flux modulation effect in the LPMV machine with a partitioned primary, the amplitudes of various harmonic components were significantly increased.

In particular, compared with the LPMV machine without a partitioned primary, the amplitudes of the 6th, 36th, and 48th harmonics of the machine with a partitioned primary were significantly increased. The 6th harmonics of the upper and lower airgap flux densities were increased by 74.2% and 78.6%, respectively, and the 36th and 48th harmonics of the lower airgap flux density were increased by 41.7% and 49.8%, respectively.

From the above analysis, the airgap flux density contains fruitful harmonics of different orders and speeds, as listed in Tab. 2. Different combinations of the modulation factors i and j modulate the different

harmonic components of the airgap flux density. Typically, a combination of i and j modulates two types of rotating modulation harmonics: $(iN_s+jP_s)^{th}$ and $(|iN_s-jP_s|)^{th}$.
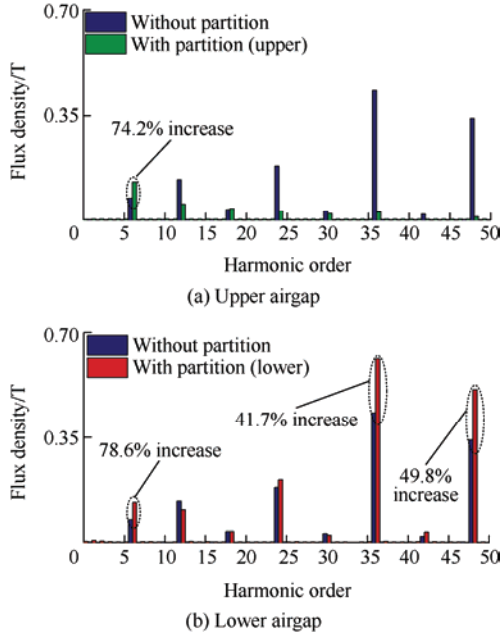

Fig. 10   Comparison of the open-circuit airgap flux densities of the two machines

Tab. 2   Classification of harmonics in the airgap PM flux density

Spatial order	Mech. speed	Elec. speed
iN_s	0	0
iN_s+jP_s	$-jP_sv/(iN_s+jP_s)$	$-jP_sv$
$iN_s-jP_s>0$	$-jP_sv/(iN_s+jP_s)$	jP_sv
$iN_s-jP_s<0$	$-jP_sv/(iN_s+jP_s)$	$-jP_sv$

4.2   Back EMF

Through the concept of the winding function, the arrangement of the armature windings can be fully considered. The single-phase winding function can be expressed as

$$N(x,t) = \sum_{m=1,3,5}^{\infty} N_m \cos\left[m\frac{2\pi}{L}P_w(x-vt) \right] \quad (13)$$

The airgap PM flux density and winding function are derived as described above. By integrating their products, the corresponding phase PM flux linkage can be expressed as

$$\psi(t) = L_{stk} \int_0^L B(x,t)N(x,t)\mathrm{d}x \quad (14)$$

where L_{stk} represents the axial lamination length of the two machines.

Furthermore, according to Faraday's law, the phase back EMF can be expressed as follows

$$e = -\frac{\mathrm{d}\psi}{\mathrm{d}t} =$$

$$\sum_{i=1}^{\infty}\sum_{j=1}^{\infty}\left[\frac{2P_smvN_pL_{stk}k_wB_{|iN_s+jP_s|}}{iN_s+jP_s}\cos(jP_svt) - \frac{2P_smvN_pL_{stk}k_wB_{|iN_s-jP_s|}}{iN_s-jP_s}\cos(jP_svt) \right] \quad (15)$$

where B represents the airgap flux density, and k_w is the winding factor.

According to Tab. 2 and Eq. (15), the contribution of the airgap PM flux-density harmonics of the two LPMV machines to the fundamental wave of the opposite potential was calculated. Because the machine with the partitioned primary has two layers of airgaps, the phase angles of the 12th, 24th, and 36th harmonics are opposite at any given time, as shown in Fig. 11. Therefore, when calculating the no-load back EMF, the magnitude of the harmonic in the opposite direction was marked as negative for processing. Tabs. 3 and 4 present the contribution of each harmonic order to the back EMF for the two machines. The analytical values of the no-load back EMF for the machines without and with the partition were 70.8 V and 98.1 V, respectively, and the corresponding FEM results were 73.4 V and 101.1 V, respectively. The errors between the results of the two methods were 3.5% and 3.0%, respectively; thus, the calculation results were relatively accurate.
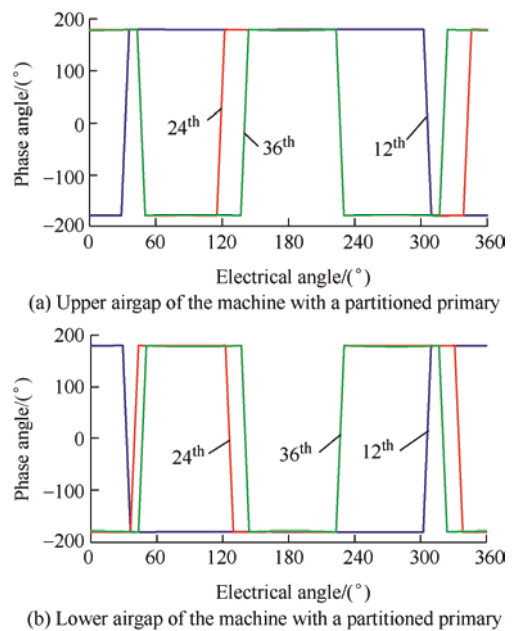

Fig. 11   Phase angles of partial harmonics

Yunpeng Xu et al.: Quantitative Comparison of Modular Linear Permanent Magnet Vernier Machines
with and without Partitioned Primary

79

Tab. 3 Fundamental phase back EMFs induced by dominant spatial harmonics for the machine without a partition

Spatial order	Amplitude/T	Back-EMF/V
6th	0.074	18.6
12th	0.136	17.1
18th	0.036	−3.0
24th	0.182	11.5
30th	0.030	−1.5
36th	0.432	18.1
42nd	0.020	−0.7
48th	0.341	10.7
Total	—	70.8

Tab. 4 Fundamental phase back EMFs induced by dominant spatial harmonics for the machine with a partition

Spatial order	Amplitude of upper airgap/T	Amplitude of lower airgap/T	Back-EMF/V
6th	0.146	0.127	68.8
12th	0.089	−0.160	−9.0
18th	0.064	0.042	−8.9
24th	−0.045	0.197	12.4
30th	0.039	0.030	−3.5
36th	−0.025	0.621	25.0
42nd	0.003	0.065	−2.5
48th	0.012	0.488	15.8
Total	—	—	98.1

Fig. 12 shows the no-load back-EMF waveforms of the two machines. Relative to the machine without a partitioned primary, the no-load back-EMF amplitude of the machine with a partitioned primary was significantly increased. Moreover, the no-load back-EMF waveforms of the two machines were sinusoidal. The total harmonic distortion rates of the back EMF were 5.3% and 5.0%, respectively.
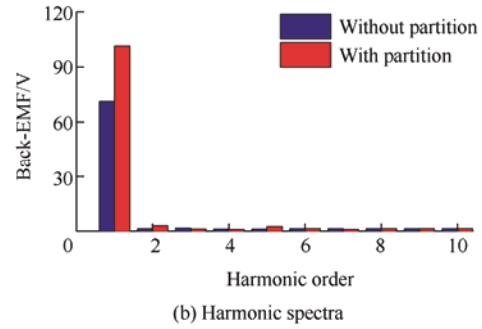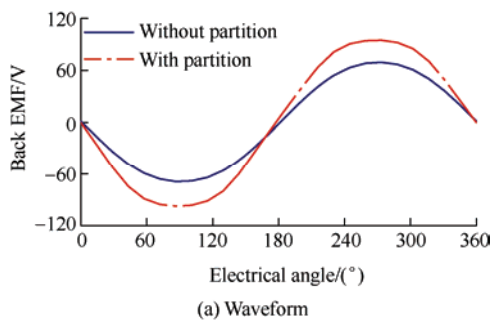

(a) Waveform

(b) Harmonic spectra

Fig. 12 Comparison of back-EMF characteristics

4.3 Inductances and forces

The two LPMV machines adopt a modular structure that can reduce the degree of coupling between phases, as shown in Fig. 13. Taking phase C of the two LPMV machines as an example, the ratios of self-inductance to mutual inductance were 1.8% and 3% for the machines without and with a partitioned primary, respectively. This indicates that the two machines had good fault tolerance. The average values of M_{cb} and M_{cd} differed from those of M_{ca}, M_{ce}, and M_{cf}. This is because there is a low-reluctance path between phase C and phases B and D.
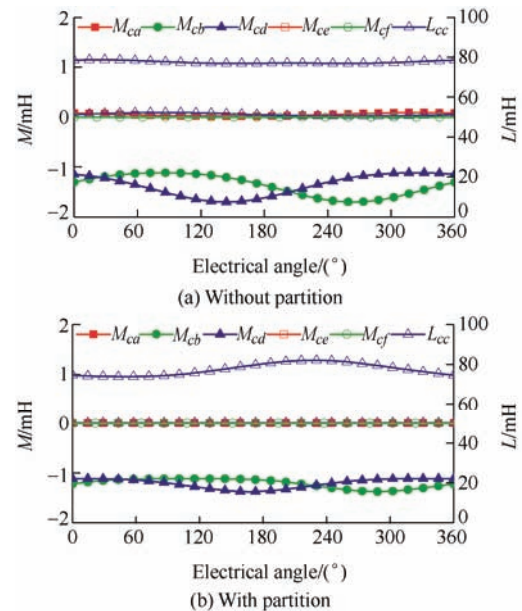

(a) Without partition

(b) With partition

Fig. 13 Inductances of the two machines

In a linear machine, a detent force does not have a positive effect on the thrust force but causes a thrust force ripple. Therefore, appropriate measures must be taken to reduce the detent forces of the machine. Fig. 14 presents the detent forces of the two LPMV machines. The two machines exhibited similar

characteristics. The waveforms of the descent forces of the six modules were similar, with an offset of 120°. The waveforms of the first and last three modules coincided. The modular primary design method can superimpose and cancel the detent forces of the modules, significantly reducing the overall descent force.

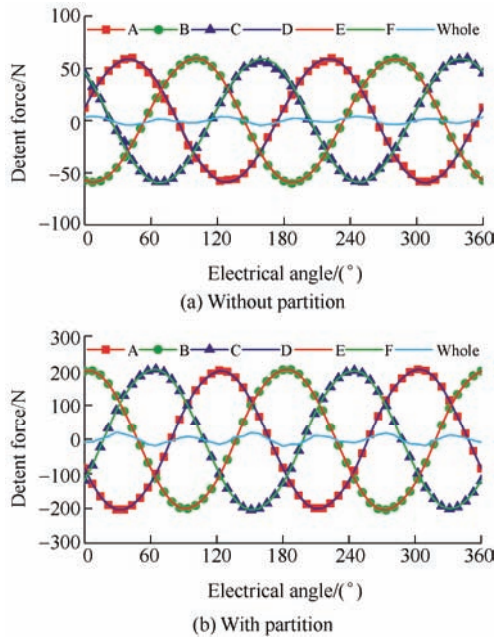(a) Without partition

(b) With partition

Fig. 14   Detent forces of the two machines

Fig. 15a presents a comparison of the thrust forces of the two machines. The results indicate that the partitioned primary can significantly increase the thrust force of the machine. Therefore, the machine with a partitioned primary has better thrust force performance than the machine without a partitioned primary. Fig. 15b presents a comparison of the average thrust force variations with respect to the current. As shown, the LPMV machine with a partition outperformed the LPMV machine without a partition in terms of the average thrust force.

(a) Position variation
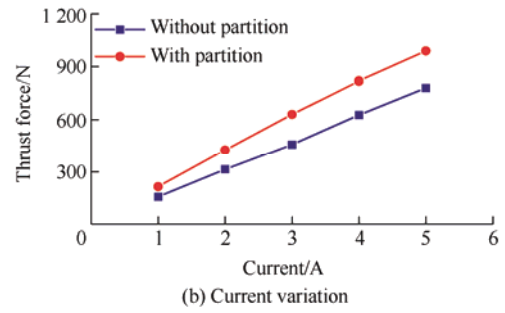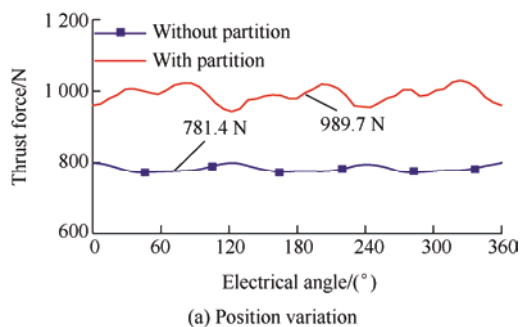

(b) Current variation

Fig. 15   Thrust forces of the two machines

5   Experimental validation

To validate the theoretical analysis results, a prototype of the reference LPMV machine was designed and manufactured. The prototype and experimental platforms are shown in Fig. 16. The no-load back EMF and thrust force calculated using the FEM were compared with the experimental results.

(a) Primary LPMV without a partition

(b) Experimental setup
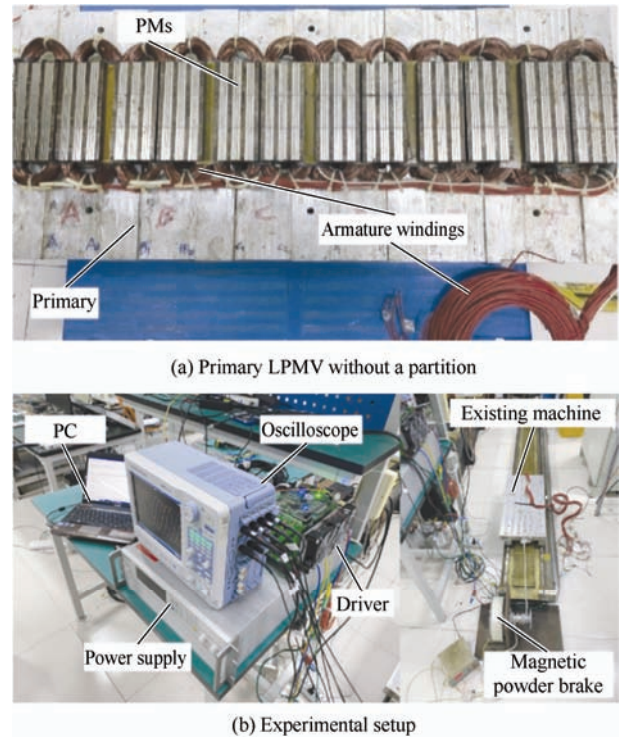
Fig. 16   Prototype and experimental platform

The phase no-load back-EMF waveforms and harmonic spectra of the prototype obtained via simulation and measurement are compared in Fig. 17. As shown, the waveform of the no-load back EMF was symmetric and sinusoidal. Additionally, the measured waveforms agreed well with the simulated waveforms. Owing to errors caused by the prototype manufacturing process, the measurement results were 4.3% lower than the simulation results.

Yunpeng Xu et al.: Quantitative Comparison of Modular Linear Permanent Magnet Vernier Machines
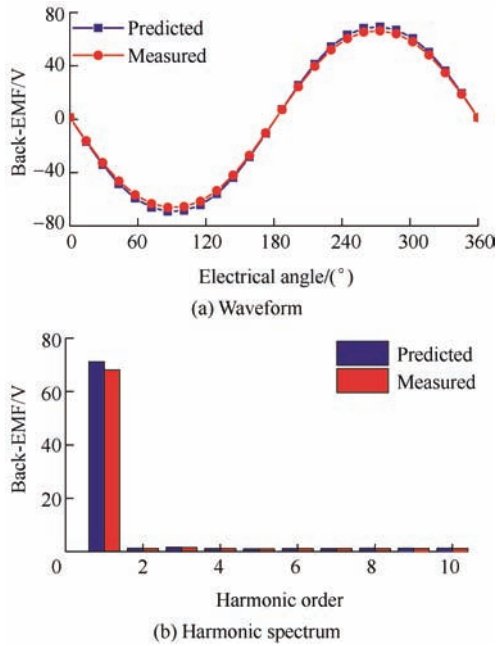with and without Partitioned Primary

81

Fig. 17　Comparison between predicted and
measured back EMFs

Fig. 18 presents a comparison of the experimental and FEM-predicted thrust forces of the LPMV machine with respect to the current. At the rated current, the error between the results obtained using the two methods was approximately 7.1%. The differences between the simulation and measurement results are acceptable, considering the effects of factors such as friction and manufacturing errors.
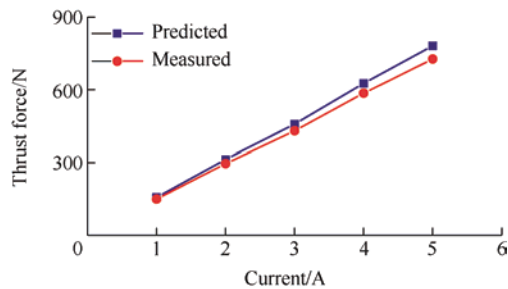

Fig. 18　Predicted and measured thrust force variations with
respect to the current

6　Conclusions

In this study, two modular LPMV machines were designed and analyzed. The effect of the partitioned primary on the modulation was evaluated from the perspective of the harmonic contribution of the flux density. The performance of the two machines was compared and analyzed. First, the topologies of the modular LPMV machines with and without a partitioned primary were introduced. Then, the

expressions of the permeance and the operation mechanism of the two machines were analyzed the flux modulation theory. In addition, the harmonic amplitude, back EMF, and thrust forces were compared and analyzed, and the internal reasons for the performance improvement were analyzed. Under the same magnetic and electrical loads, the thrust force density of the machine with the partitioned primary was significantly higher (by approximately 32.3%). Finally, detailed tests were conducted on the prototype to verify the accuracy of the theoretical analysis and simulation results. Owing to the innovative combination of the modular design and partitioned primary, the LPMV machine with partitioning has the advantages of a low cost, small thrust force ripple, and high thrust force density. Therefore, it is suitable for rail transit traction systems and other applications.

References

[1] R A H de Oliveira, R M Stephan, A C Ferreira, et al. Design and innovative test of a linear induction motor for urban maglev vehicles. *IEEE Transactions on Industry Applications*, 2020, 56(6): 6949-6956.

[2] W Xu, X Xiao, G Du, et al. Comprehensive efficiency optimization of linear induction motors for urban transit. *IEEE Transactions on Vehicular Technology*, 2020, 69(1): 131-139.

[3] J Ge, W Xu, Y Liu, et al. Investigation on winding theory for short primary linear machines. *IEEE Transactions on Vehicular Technology*, 2021, 70(8): 7400-7412.

[4] P Naderi, A Shiri. Modeling of ladder-secondary-linear induction machine using magnetic equivalent circuit. *IEEE Transactions on Vehicular Technology*, 2018, 67(12): 11411-11419.

[5] W Wang, J Zhao, Y Zhou, et al. New optimization design method for a double secondary linear motor based on R-DNN modeling method and MCS optimization algorithm. *Chinese Journal of Electrical Engineering*, 2020, 6(3): 98-105.

[6] S G Min. Integrated design method of linear PM machines considering system specifications. *IEEE Transactions on Transportation Electrification*, 2021, 7(2): 804-814.

[7] B Ullah, F Khan, S Hussain, et al. Modeling, optimization, and analysis of segmented stator flux switching linear hybrid excited machine for electric power train. *IEEE Transactions on Transportation Electrification*, 2022, 8(3): 3546-3553.

[8] J Wang, W Wang, K Atallah. A linear permanent-magnet motor for active vehicle suspension. *IEEE Transactions on Vehicular Technology*, 2011, 60(1): 55-63.

[9] Z Zhao, G Ma, J Luo, et al. Modeling and characteristic analysis of air-cored linear synchronous motors with racetrack coils for electrodynamic suspension train. *IEEE Transactions on Transportation Electrification*, 2022, 8(2): 1828-1838.

[10] Q Ge, B Kou, H Zhang, et al. Secondary eddy current losses reduction in a double-sided long-primary fractional slot concentrated winding permanent magnet linear synchronous motor. *IEEE Transactions on Industrial Electronics*, 2022, 69(5): 5018-5029.

[11] Q Tan, M Wang, L Li. Analysis of a new flux switching permanent magnet linear motor. *IEEE Transactions on Magnetics*, 2021, 57(2): 8201705.

[12] P Naderi, M Heidary. A novel permanent magnet flux-switching linear motor performance analysis by flexible MEC method. *IEEE Transactions on Energy Conversion*, 2021, 36(3): 1910-1918.

[13] B Kou, J Luo, X Yang, et al. Modeling and analysis of a novel transverse-flux flux-reversal linear motor for long-stroke application. *IEEE Transactions on Industrial Electronics*, 2016, 63(10): 6238-6248.

[14] Y Shen, T Shi, Q Lu, et al. Robust design and analysis of asymmetric-excited flux reversal PM linear machine for long-stroke direct drive propulsion. *IEEE Transactions on Magnetics*, 2021, 57(6): 8106104.

[15] R Cao, D Shen, W Hua. Research on detent force characteristics of a linear flux-switching permanent-magnet motor. *IEEE Transactions on Energy Conversion*, 2021, 36(4): 2998-3006.

[16] L Zhang, L Wu, H Wen, et al. Improved primary/secondary pole number combinations for dual-armature linear switched flux permanent magnet machines. *IEEE Transactions on Transportation Electrification*, 2021, 7(4): 2589-2599.

[17] G Liu, H Zhong, L Xu, et al. Analysis and evaluation of a linear primary permanent magnet vernier machine with multiharmonics. *IEEE Transactions on Industrial Electronics*, 2021, 68(3): 1982-1993.

[18] M Ghods, J Faiz, M A Bazrafshan, et al. A mesh design technique for double stator linear PM vernier machine based on equivalent magnetic network modeling. *IEEE Transactions on Energy Conversion*, 2022, 37(2): 1087-1095.

[19] W Zhao, J Zheng, J Wang, et al. Design and analysis of a linear permanent- magnet vernier machine with improved force density. *IEEE Transactions on Industrial Electronics*, 2016，63(4): 2072-2082.

[20] M Wang, L Li, R Yang. Overview of thrust ripple suppression technique for linear motors. *Chinese Journal of Electrical Engineering*, 2016, 2(1): 77-84.

[21] F Yan, J Ji, Z Ling, et al. Magnets shifting design of dual PM excited vernier machine for high-torque application. *Chinese Journal of Electrical Engineering*, 2022, 8(3): 90-101.

[22] Y Shi, T W Ching, J Zhong, et al. A dual-stator HTS modular linear vernier motor for long stroke applications. *IEEE Transactions on Industry Applications*, 2022, 32(6): 1-8.

[23] K Wang, F Li, H Y Sun, et al. Consequent pole permanent magnet machine with modular stator. *IEEE Transactions on Vehicular Technology*, 2020, 69(7): 7054-7063.

[24] W Zhao, T Yao, L Xu, et al. Multi-objective optimization design of a modular linear permanent-magnet vernier machine by combined approximation models and differential evolution. *IEEE Transactions on Industrial Electronics*, 2021, 68(6): 4634-4645.

[25] F Bian, W Zhao, J Ji, et al. Mechanism investigation of ring type winding in linear permanent magnet vernier machine for improving force density. *IEEE Transactions on Vehicular Technology*, 2020, 69(3): 2588-2597.

[26] W Zhao, S Wang, J Ji, et al. A new mover separated linear magnetic-field modulated motor for long stroke applications. *IEEE Transactions on Magnetics*, 2017, 53(11): 8202604.

[27] Q Lu, B Wu, Z Zeng, et al. Analysis of a new partitioned-primary flux-reversal hybrid-excited linear motor. *IEEE Transactions on Industry Applications*, 2021, 57(1): 448-457.

[28] Z Zeng, Q Lu. Investigation of novel partitioned-primary hybrid-excited flux-switching linear machines. *IEEE Transactions on Industrial Electronics*, 2018, 65(12): 9804-9813.

Yunpeng Xu received a B.Sc. degree in Automation from Jiangsu University, Zhenjiang, China in 2020. He is currently working toward an M.Sc. degree in Control Engineering at Jiangsu University, Zhenjiang, China.

His research interests include machine design and magnetic-field modulation analysis.

Yunpeng Xu et al.: Quantitative Comparison of Modular Linear Permanent Magnet Vernier Machines
with and without Partitioned Primary

83

Jinghua Ji received B.Sc., M.Sc., and Ph.D. degrees in Electrical Engineering from Jiangsu University, Zhenjiang, China in 2000, 2003, and 2009, respectively.

Since 2000, she has been affiliated with the School of Electrical and Information Engineering, Jiangsu University, where she is currently a Professor. From 2013 to 2014, she was a Visiting Scholar with the Department of Electronic and Electrical Engineering, The University of Sheffield, Sheffield, UK. She has authored or coauthored over 50 technical papers in these areas. Her research interests include electrical machines and motor drives.

Zhijian Ling received a B.Sc. degree in Electrical Engineering and Automation from Shandong Agriculture University, Tai'an, China, in 2013, and a Ph.D. in Electrical Engineering from Jiangsu University, Zhenjiang, China, in 2020. He is currently a Lecturer with the School of Electrical and Information Engineering, Jiangsu University.

His research interests include the design and analysis of machines, including electrical actuators.

Chen Wang received a B.Sc. degree in Electronic Information Science and Technology from Jiangsu University, Zhenjiang, China in 2015, where he is currently working toward a Ph.D. in Agricultural Engineering.

His research interests include power converters and permanent-magnet motor drives.

Wenxiang Zhao (M'08-SM'14) received B.Sc. and M.Sc. degrees in Electrical Engineering from Jiangsu University, Zhenjiang, China in 1999 and 2003, respectively, and a Ph.D. in Electrical Engineering from Southeast University, Nanjing, China in 2010.

He has been affiliated with Jiangsu University since 2003, where he is currently a Professor with the School of Electrical Information Engineering. From 2008 to 2009, he was a Research Assistant with the Department of Electrical and Electronic Engineering, The University of Hong Kong, Hong Kong, China. From 2013 to 2014, he was a Visiting Professor with the Department of Electronic and Electrical Engineering, The University of Sheffield, Sheffield, UK. He has authored and coauthored over 150 papers published in various IEEE Transactions. His research interests include electric machine design, modeling, fault analysis, and intelligent control.